

A state-based peridynamic model for quantitative fracture analysis

Heng Zhang · Pizhong Qiao 

Received: 13 August 2017 / Accepted: 8 April 2018 / Published online: 7 May 2018
© Springer Science+Business Media B.V., part of Springer Nature 2018

Abstract A new state-based peridynamic model is proposed to quantitatively analyze fracture behavior (crack initiation and propagation) of materials. In this model, the general relationship of the critical stretch and the critical energy release rate is for the first time obtained for the state-based peridynamic model of linear elastic brittle materials, and the released energy density is defined to quantitatively track the energy released during crack propagation. The three-dimensional (3D) and two-dimensional (2D) (for both plane stress and plane strain) cases are all considered. As illustrations, the compact tension and double cantilever beam tests are analyzed using the proposed model, which is capable of successfully capturing fracture behaviors (e.g., crack path and concentration of strain energy density) of the considered fracture tests. The characteristic parameters (i.e., critical load, critical energy release rate, etc.) are calculated and compared with available experimental and numerical data in the literature to demonstrate validity of the proposed model.

Keywords Peridynamics · State-based model · Critical stretch · Bond failure

1 Introduction

It is significant in engineering design to accurately predict fracture behavior of materials. Although experimental tests remain the best way to catch accurate results, numerical tools are much effective for complex structures with less cost. Thus, numerical prediction of crack growth has attracted much attention.

Most used numerical methods, e.g., finite element method (FEM), are naturally unsuitable to fracture analysis because of its requirement of displacement continuity for classical continuum mechanics. Various remedies, such as extended finite element method (Belytschko and Black 1999), were proposed to handle the shortcoming of FEM. Though the XFEM has been successfully applied for a number of fracture problems, the external criteria (Baydoun and Fries 2012) are still needed when it is employed to intricate problems. The theory of peridynamics was first proposed by Silling (2000) to overcome the limitations of classical continuum mechanics, particularly in dealing with discontinuity problems. Instead of partial differential equations used in the governing equations of continuum mechanics, the integral-differential equations are established in peridynamics to avoid the displacement derivatives, which are not defined in discontinuous field. Thus, the peridynamic model can effectively handle discontinuity problems, such as crack initiation and propagation.

H. Zhang · P. Qiao (✉)
State Key Laboratory of Ocean Engineering, Collaborative
Innovation Center for Advanced Ship and Deep-Sea
Exploration, School of Naval Architecture, Ocean and Civil
Engineering, Shanghai Jiao Tong University, Shanghai
200240, People's Republic of China
e-mail: qiao@sjtu.edu.cn;
qiao@wsu.edu

P. Qiao
Department of Civil and Environmental Engineering, Wash-
ington State University, Sloan Hall 117, Pullman, WA 99164-2910,
USA

The first proposed peridynamic (PD) model, so called “bond-based” (Silling 2000), assumes that points are connected with bonds through spring-like interactions and the response in a bond is independent of any other bonds. However, this assumption has constraints on material properties and restricts the types of materials. More general formulation was proposed as state-based peridynamic model (Silling et al. 2007), and the bond force density between points depends on the deformation of the points of whole family. In addition, a two-dimensional ordinary, state-based peridynamic model (Le et al. 2014) was proposed for linear elastic solids.

While peridynamics was primarily proposed to deal with the problems involving discontinuities, the suitable damage models are necessary and important for quantitative analysis of fracture problems. Silling and Askari (2005) first proposed the bond damage criterion for prototype microelastic brittle material and presented the relationship between the critical stretch for bond failure and the critical energy release rate of material. This model was used to analyze dynamic brittle fracture (Ha and Bobaru 2011), and it was later extended for damage predictions of concrete (Gerstle et al. 2007), composite material (Xu et al. 2007), orthotropic media (Ghajari et al. 2014), interface delamination (Hu et al. 2015), and bimaterial structures (Zhang and Qiao 2018). Furthermore, Hu et al. (2012) presented the formulation of the J-intergral in the framework of bond-based peridynamics.

However, the aforementioned damage models for fracture analysis were all proposed using the bond-based peridynamic model. In the state-based peridynamic model, two connected points affect each other with collection of the deformation of the entire family. But the existing damage model in the framework of bond-based peridynamics model is not feasible for peridynamic state. Instead, Foster et al. (2011) proposed an energy-based failure criterion which can be used in peridynamic state, and the critical energy density for bond failure was defined and derived from the critical energy release rate of material. However, it is not easy to calculate the strain energy density stored in each neighboring bond in the state-based peridynamic model because of the nonlinear relationship between force scaler and extension scaler of the bond. Thus, it is necessary to develop state-based peridynamic model for fracture analysis and obtain new form of critical stretch in the context of state-based

peridynamic model for potential quantitative fracture analysis.

In this paper, a peridynamic damage model for fracture analysis is proposed with the new form of critical stretch considering peridynamic state, and the fracture tests using the compact tension (CT) and double cantilever beam (DCB) specimens are quantitatively analyzed. First, the general state-based peridynamic model applicable for both the 3D and 2D cases is presented, and the relationship between the state-based and bond-based peridynamic models is introduced. A state-based peridynamic damage model for linear elastic brittle materials is proposed, and the new form of critical stretch considering peridynamic state is given. The parameter of energy release density is defined to quantitatively track the energy released during crack propagation. The quantitative fracture analysis and convergence study of the CT test are performed using the crack length (a) to specimen width (w) ratio $a/w = 0.5$, followed by the damage predictions of the CT specimens with different values of a/w . While fracture behavior of DCB test is analyzed with the proposed damage model, the critical load predictions of DCB specimens with different crack lengths are discussed. The characteristic parameters (e.g., critical load and critical energy release rate) are calculated and compared with available experimental and numerical data in the literature.

2 Review of peridynamic models

In the general state-based peridynamic model (Silling et al. 2007), the equation of motion of the material point \mathbf{x} is:

$$\rho(\mathbf{x}) \ddot{\mathbf{u}}(\mathbf{x}, t) = \int_{H_{\mathbf{x}}} \{ \underline{\mathbf{T}}[\mathbf{x}, t] \langle \mathbf{x}' - \mathbf{x} \rangle - \underline{\mathbf{T}}[\mathbf{x}', t] \langle \mathbf{x} - \mathbf{x}' \rangle \} dV_{\mathbf{x}'} + \mathbf{b}(\mathbf{x}, t) \quad (1)$$

where $H_{\mathbf{x}}$ is the neighborhood of point \mathbf{x} , ρ is the density, and \mathbf{u} is the displacement of \mathbf{x} at time t . \mathbf{x}' is the material point in the neighborhood of \mathbf{x} , and $\mathbf{b}(\mathbf{x}, t)$ is the body force density of the point \mathbf{x} . As shown in Fig. 1, $\underline{\mathbf{T}}[\mathbf{x}, t]$ and $\underline{\mathbf{T}}[\mathbf{x}', t]$ are the force vector states that show the constitutive models of points \mathbf{x} and \mathbf{x}' , respectively.

In this section, a general state-based peridynamic model available for both the 3D and 2D cases is first presented. The relationship between the state-based and bond-based peridynamic models is discussed.

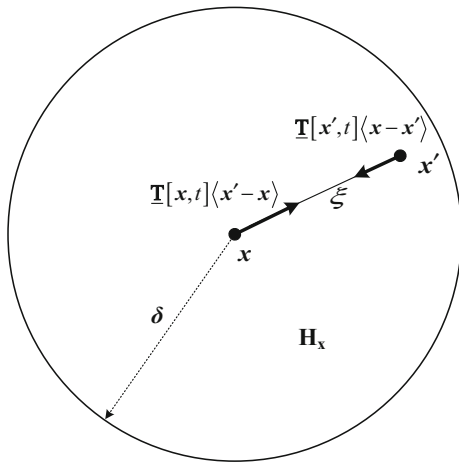


Fig. 1 Ordinary state-based peridynamic model

2.1 General peridynamic model

For the linear elastic isotropic material, the general strain energy density of material point x in the peridynamic model can be expressed as (Silling 2000):

$$W = \frac{a\theta^2}{2} + \frac{b}{2} (\underline{\omega e^d}) \cdot \underline{e^d} \tag{2}$$

where a and b are the peridynamic constants, respectively. $\underline{\omega}$ is the influence function, θ is the volume dilatation, and $\underline{e^d}$ is the deviatoric extension state. The dot product (\cdot) is defined in Silling (2010). As described in Silling (2010), those parameters in the case of 3D take forms of:

$$\theta = 3 \frac{\underline{\omega x} \cdot \underline{e}}{q}, \quad \underline{e^d} = \underline{e} - \theta \underline{x}/3, \quad a = k, \quad b = \frac{15\mu}{q} \tag{3}$$

where k and μ are the bulk and shear modulus, respectively. \underline{x} is the scalar state whose value at the position $\underline{\xi}$ is the scalar bond length $|\underline{\xi}|$, \underline{e} is the extension scalar state, and q is the weighted volume defined by $q = (\underline{\omega x}) \cdot \underline{x}$.

The scalar force state \underline{t} of the 3D peridynamic model for elastic solid material is (Silling 2010):

$$\underline{t} = 3k\theta \frac{\underline{\omega x}}{q} + \frac{15\mu}{q} \underline{\omega e^d} \tag{4}$$

Unlike the definitions of the 2D peridynamic model in Le et al. (2014), the different forms of θ and $\underline{e^d}$ in this study are used as:

$$\theta = 2 \frac{\underline{\omega x} \cdot \underline{e}}{q}, \quad \underline{e^d} = \underline{e} - \theta \underline{x}/2 \tag{5}$$

Then, following the same deduction steps in Silling (2010), the expressions of a and b for 2D peridynamic model have different values as:

$$a = k', \quad b = \frac{8\mu}{q} \tag{6}$$

where k' is the two-dimensional (2D) bulk modulus that can be expressed in terms of the elastic modulus E and the Poisson's ratio ν as:

$$k' = \begin{cases} \frac{E}{2(1-\nu)} & \text{Plane stress} \\ \frac{E}{2(1+\nu)(1-2\nu)} & \text{Plane strain} \end{cases} \tag{7}$$

And the form of scalar force state \underline{t} for 2D peridynamic model can be expressed as:

$$\underline{t} = 2k'\theta \frac{\underline{\omega x}}{q} + \frac{8\mu}{q} \underline{\omega e^d} \tag{8}$$

Thus, in the 2D peridynamic model, by using the different definitions of θ and $\underline{e^d}$ in Eq. (5), the peridynamic energy density of Eq. (2) and the scalar force state of Eq. (8) have the different formations as those in Le et al. (2014). However, it can be proven that two kinds of forms are equal, and these forms in Eqs. (2) and (8) are much simple and easy to compute.

Generally, using the definitions of Eqs. (3) and (5), the strain energy density of peridynamic model in Eq. (2) can be rewritten as (Silling 2010):

$$W = \frac{1}{2} a' \theta^2 + \frac{b}{2} (\underline{\omega e}) \cdot \underline{e} \tag{9}$$

where a' is defined as:

$$a' = \begin{cases} a - \frac{bq}{9} & 3D \\ a - \frac{bq}{4} & 2D \end{cases} \tag{10}$$

where a and b are given in Eqs. (3) and (6) for the cases of 3D and 2D, respectively. The form of scalar force

state \underline{t} can then be rewritten as:

$$\underline{t} = (a'\theta) \nabla_e \theta + b\omega e \tag{11}$$

where $\nabla_e \theta$ is the Frechet derivative of θ with respect to e . According to the definition of the Frechet derivative (Silling et al. 2007) and using the forms of θ in Eqs. (3) and (5), $\nabla_e \theta$ can be written as:

$$\nabla_e \theta = \begin{cases} 3 \frac{\omega x}{q} & 3D \\ 2 \frac{\omega x}{q} & 2D \end{cases} \tag{12}$$

In summary, the general expressions of the strain energy density and scalar force state are given in Eqs. (9) and (11), respectively, and they are available for both the 3D and 2D cases with the respective parameters.

2.2 Relationship between the state-based and bond-based peridynamic models

For the bond-based peridynamic model, there are restrictions on the values of the Poisson's ratio as (Silling 2000):

$$v = \begin{cases} \frac{1}{3} & \text{Plane stress} \\ \frac{1}{4} & \text{3D or Plane strain} \end{cases} \tag{13}$$

Substituting these constrained values of v into the definition of a' in Eq. (10) leads to a' equaling to 0. Then, the forms of strain energy density in Eq. (9) and scalar force state in Eq. (11) can be reduced as:

$$W = \frac{b}{2} (\omega e) \cdot e, \quad \underline{t} = b\omega e \tag{14}$$

Specially, if the influence function takes the form of $\omega = \delta/x$, which is then substituted in the forms of b , and the value of v in Eq. (13) is used, the forms in Eq. (14) can be rewritten as:

$$W = \frac{1}{2} \int_{H_x} \frac{1}{2} C \underline{s}^2 \underline{x} dV_\xi = \frac{1}{2} \int_{H_x} w_\xi dV_\xi, \\ \underline{t} = \frac{1}{2} C \underline{s} = \frac{1}{2} f \tag{15}$$

where the bond stretch scaler state \underline{s} is defined as $\underline{s} = e/x$, w_ξ and f are the micropotential and scalar bond force of bond ξ in the bond-based peridynamic model

(Silling and Askari 2005), and C is the bond constant which has the values of:

$$C = \begin{cases} \frac{18k}{\pi \delta^4} & 3D \\ \frac{12k'}{\pi \delta^3 h} & 2D \end{cases} \tag{16}$$

Until now, the forms of strain energy density and scalar force state are reduced to the expressions given in Eq. (15) with the constrained values of v and special form of influence function, and the forms of w_ξ and f are totally equal to those of the bond-based peridynamic model in Silling and Askari (2005) and Ha and Bobaru (2011) for the cases of 3D and 2D, respectively. Thus, the bond-based model can be regarded as a special case of state-based model.

3 State-based peridynamic model for fracture analysis

In this section, a state-based peridynamic model for fracture analysis of linear elastic brittle materials is proposed, and more general relationship of the critical stretch for bond failure with the critical energy release rate of material commonly used in linear elastic fracture mechanics (LEFM) is for the first time established.

Unlike the bond-based peridynamic model, there is no real bond between pair points in the state-based peridynamics. The bond here is used loosely to describe the relationship between pair points and can be thought as an interaction potential (Foster et al. 2011), and the bond stretch criterion thus still works. When the deformation of bond between the two points grows beyond the critical stretch value, the bond permanently breaks and the crack will initiate and grow when a number of broken bonds coalesce into a surface and propagate.

Similarly to Silling and Askari (2005), as shown in Fig. 2, the points x and x' are connected with the bond ξ , and the H_1 domain is cut by the crack area from the whole horizon domain which is a sphere or circle in the cases of 3D or 2D, respectively. According to the form of peridynamic strain energy density in Eq. (9), the strain energy of point x gathers from other points in its horizon through those bonds. When the bond stretch \underline{s} of ξ grows beyond the critical stretch s_0 , the bond ξ is broken and the part of strain energy of point x gathering from point x' is lost or released. As the crack grows or propagates, all bonds connecting the point x with the points x' in H_1 are all broken, and the corresponding

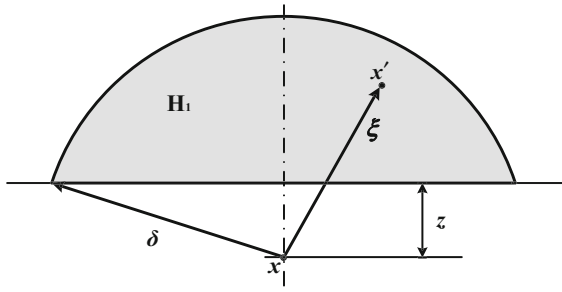


Fig. 2 Computation of the total energy absorbed by point x in the domain H_1

part of strain energy of the point x gathering from all points in the H_1 domain is thus released. Now, assume that the work requiring the point x to separate with all the neighboring points in H_1 is equal to the strain energy released as the crack grows.

To compute the released energy of point x , assuming that the bond stretch of all bonds ξ across the crack area all arrives the critical stretch s_0 , the extension scaler is $\underline{e} = s_0 \underline{x}$.

For 3D peridynamic model, according to the definition of θ in Eq. (3), the volume dilation caused by all broken bond is:

$$\tilde{\theta}_s = 3 \frac{\underline{\omega x} \cdot \underline{e}}{q} = 3 \frac{\int_{H_1} \underline{\omega x}^2 s_0 dV_\xi}{\int_H \underline{\omega x}^2 dV_\xi} = 3\lambda(z)s_0 \quad (17)$$

where $\lambda(z)$ is the ratio of the volume weight from the points in the H_1 domain to the volume weight from the points in the whole horizon, defined as:

$$\lambda(z) = \frac{\int_{H_1} \underline{\omega x}^2 dV_\xi}{\int_H \underline{\omega x}^2 dV_\xi} \quad (18)$$

Substituting Eq. (18) into the strain energy density of Eq. (9) leads to the released energy of a point x because of the crack growth as:

$$\begin{aligned} W_x &= \frac{a'}{2} \tilde{\theta}_s^2 + \frac{b}{2} \int_{H_1} \underline{\omega x}^2 s_0^2 dV_\xi \\ &= \frac{1}{2} \left(9a'\lambda(z)^2 + bq\lambda(z) \right) s_0^2 \end{aligned} \quad (19)$$

Thus, the total released energy at unit area is:

$$\begin{aligned} dU_e &= 2 \int_0^\delta dW_x dz = 2 \int_0^\delta \frac{1}{2} \left(9a'\lambda(z)^2 + bq\lambda(z) \right) s_0^2 dz \\ &= (9a'\beta' + bq\beta) s_0^2 \end{aligned} \quad (20)$$

The first two multipliers of 2 in Eq. (20) is for the double side of the crack because of the homogeneous nature of the body, where β and β' are the certain parameters which are affected by the influence function, defined as:

$$\beta = \int_0^\delta \lambda(z) dz, \quad \beta' = \int_0^\delta \lambda(z)^2 dz \quad (21)$$

The total released energy at unit area is equal to the critical energy release rate or fracture energy G_0 , and it is expressed as:

$$G_0 = dU_e = (9a'\beta' + bq\beta) s_0^2 \quad (22)$$

So, the critical stretch (s_0) of state-based peridynamic model for 3D is uniquely obtained in term of the critical energy release rate (G_0) as:

$$s_0 = \sqrt{G_0 / (9a'\beta' + bq\beta)} \quad (23)$$

In the cases of 2D, following the same deductions and using different peridynamic parameters in Eqs. (5) and (6), the released energy of point x and total released energy at unit area take the forms of:

$$\begin{aligned} W_x &= \frac{1}{2} \left(4a'\lambda(z)^2 + bq\lambda(z) \right) s_0^2, dU_e \\ &= (4a'\beta' + bq\beta) s_0^2 \end{aligned} \quad (24)$$

Then, the critical stretch of state-based peridynamics model for 2D cases can be written as:

$$s_0 = \sqrt{G_0 / (4a'\beta' + bq\beta)} \quad (25)$$

As a whole, substituting a' in Eq. (10), a and b in Eqs. (3) and (5) into Eqs. (23) and (25) for the cases of 3D and 2D model, respectively, the critical stretch of state-based peridynamic model can totally be rewritten as:

$$s_0 = \begin{cases} \sqrt{G_0 / ((9k - 15\mu)\beta' + 15\mu\beta)} & 3D \\ \sqrt{G_0 / ((4k' - 8\mu)\beta' + 8\mu\beta)} & 2D \end{cases} \quad (26)$$

where β and β' are defined in Eq. (21), which are based on the definition of $\lambda(z)$ in Eq. (18). The values of β and β' are the certain parameters which are decided by the horizon size δ , the form of influence function, and the dimension of the model. Specifically, when the influence function takes the form of $\underline{\omega} = \delta/\underline{x}$ which

is substituted to Eq. (21), the values of β and β' are computed using Matlab and then given as:

$$3D : \begin{cases} \beta = \frac{\delta}{5} \\ \beta' = \frac{26}{405}\delta \end{cases}, \quad 2D : \begin{cases} \beta = \frac{3\delta}{4\pi} \\ \beta' = 0.23873\delta \end{cases} \quad (27)$$

For the bond-based peridynamic model, there are restrictions on the Poisson’s ratio. Substituting the values of ν in Eq. (13) into Eq. (26) and using Eq. (27), the forms of critical stretch in the bond-based peridynamic model are recovered as:

$$s_0 = \begin{cases} \sqrt{\frac{5G_0}{9k\delta}} & 3D \\ \sqrt{\frac{\pi G_0}{3k'\delta}} & 2D \end{cases} \quad (28)$$

These forms of the critical stretch in Eq. (28) are just identical to the forms given in Silling and Askari (2005) and Ha and Bobaru (2011) for the cases of 3D and 2D, respectively, as typically proposed for the bond-based peridynamic model. Particularly, for the mode I type crack, the critical energy release rate G_{IC} can be calculated from Sun and Jin (2013) as:

$$G_{IC} = \begin{cases} \frac{(1-\nu^2)}{E} K_{IC}^2 & \text{Plane strain} \\ \frac{1}{E} K_{IC}^2 & \text{Plane stress} \end{cases} \quad (29)$$

In summary, the general relationship of the critical stretch with respect to the critical energy release rate in LEFM is for the first time obtained in Eq. (26) for the state-based peridynamic model. The 3D, plane stress and plane strain cases are all considered. Unlike the fracture analysis for the bond-based model as given in Silling and Askari (2005) and Ha and Bobaru (2011), the critical stretch for the state-based model takes the varying values of the Poisson’s ratio into account. As a validation, the proposed state-based peridynamic model for fracture analysis can be further reduced to the bond-based damage model with the typical influence function and constrained values of the Poisson’s ratio. Also, unlike the critical stretch given in Madenci and Oterkus (2014) which is in the discrete form and with the special form of influence function, the new form in Eq. (26) developed in this study is in a general form for the state-based peridynamics and suitable to any reasonable influence function.

In addition, the forms of released energy of a point are given in Eqs. (19) and (24) for 3D and 2D

cases, respectively. The variable parameter of point, i.e., released energy density, is defined to quantify the released energy as crack grows. The value of released energy density is equal to the released energy of a point, and the summation of the released energy density of system is equal to the total incremental surface energy. However, the released energy density is not a real physical energy, rather than the division of total released energy into the points around crack when crack propagates because of the non-local characteristic of peridynamic model.

Since the crack initiates and grows spontaneously in peridynamic fracture simulation, there is no explicit gap point of time between stable load before crack initiation and the increasing load as crack propagates. To track the zero time when the crack begins to grow, the critical time t_c is defined. According to the forms of released energy density in Eqs. (19) and (24), the total released energy increases progressively with the increasing number of broken bonds. At the stage of the crack initiation, even some bonds around the pre-crack tip are broken, the system is stable to undertake the displacement load. Until the total released energy increases beyond a critical value, the crack starts to propagate. Thus, the critical released energy is defined as:

$$w_s = \frac{1}{2} G_0 B \Delta x \quad (30)$$

where Δx and B are the grid size and thickness of model ahead the crack tip, respectively. And the critical time t_c is defined as

$$t_c = t_0, \quad \text{if } W_S(t_0) = w_s \quad (31)$$

where $W_S(t_0)$ is the total released energy (the incremental surface energy) of system in the time t_0 . Thus, the critical time t_c is recorded when $W_S(t_0)$ increases to be equal to the critical released energy w_s , and it is proven to be the time when the crack starts to propagate.

4 Numerical implementation

Similarly to Silling and Askari (2005), the continuum system is discretized into the finite material nodes, and each node has a finite volume. The equation of motion

in Eq. (1) can thus be rewritten as:

$$\rho_i \ddot{u}_i(x_i, t) = \sum_{j \in H_i} \{T[x_i, t] \langle x_j - x_i \rangle - T[x_j, t] \langle x_i - x_j \rangle\} V_j + b_i(x_i, t) \tag{32}$$

where i and j are the node numbers, and V_j is the volume of node j . In all the examples followed, the uniform grid size Δx is used. The summation of Eq. (32) is taken over the horizon H_i of node i as $|x_j - x_i| \leq \delta$, where δ is the horizon size as $\delta = m \Delta x$.

For the peridynamic simulations, the explicit (Silling and Askari 2005) and implicit (Zhang et al. 2016) time integration methods are usually used for dynamic and static analysis, respectively. In the following examples, the brittle damage process is simulated and the explicit time integration Velocity-Verlet algorithm (Hairer et al. 2003) is employed.

A paralleled C++ program has been developed to numerically solve the peridynamic equations. In the present work, all examples are run on a 24-core workstation running Linux.

5 Application to fracture specimens

In this section, the standard compact tension (CT) (ASTM E399-12 2013) and double cantilever beam (DCB) (ASTM D5528-01 2001) tests commonly for fracture characterization are considered to demonstrate and validate the proposed state-based peridynamic damage model.

5.1 Compact tension (CT) test

5.1.1 Problem

setup and computational detail for CT test

The CT test (ASTM E399-12 2013) is usually used to determine the critical energy release rate of linear elastic isotropic metallic material. The CT specimen can be schematically shown in Fig. 3.

From the standard of test (ASTM E399-12 2013), the relationship of the critical stress intensity factor, K_{IC} , and the maximum crack propagation load, P_c , can be shown as:

$$K_{IC} = \frac{P_c}{B w^{1/2}} f\left(\frac{a}{w}\right), \tag{33}$$

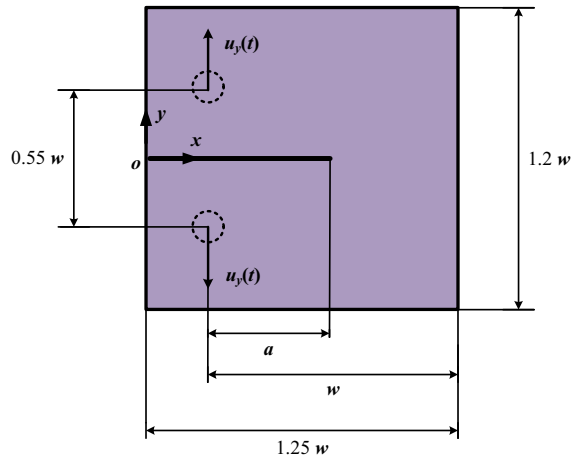


Fig. 3 The CT specimen

where

$$f\left(\frac{a}{w}\right) = \frac{(2 + \frac{a}{w}) \left[0.886 + 4.46 \frac{a}{w} - 13.32 \left(\frac{a}{w}\right)^2 + 14.72 \left(\frac{a}{w}\right)^3 - 5.6 \left(\frac{a}{w}\right)^4 \right]}{\left(1 - \frac{a}{w}\right)^{3/2}} \tag{34}$$

as shown in Fig. 3, a and w are the crack length and width of the specimen, respectively, and B is the thickness of the specimen. The crack mouth opening compliance is calculated as:

$$\frac{V_m}{P_c} = \frac{1}{E' B} q\left(\frac{a}{w}\right) \tag{35}$$

where

$$q\left(\frac{a}{w}\right) = \frac{19.75}{\left(1 - \frac{a}{w}\right)^2} \left[0.5 + 0.192 \frac{a}{w} + 1.385 \left(\frac{a}{w}\right)^2 - 2.919 \left(\frac{a}{w}\right)^3 + 1.842 \left(\frac{a}{w}\right)^4 \right] \tag{36}$$

for which V_m is the crack mouth opening displacement at point o in Fig. 3, and:

$$E' = \begin{cases} \frac{E}{(1-\nu^2)} & \text{Plane strain} \\ E & \text{Plane stress} \end{cases} \tag{37}$$

In summary, the critical values of applied load and crack mouth opening compliance for the standard CT test can be obtained in Eqs. (33) and (35), respectively. Since the expressions for a/w in Eqs. (34) and (36) are considered to be accurate within 1% over the range

$0.2 \leq a/w \leq 1.0$ (ASTM E399-12 2013), the equations can be used as the standard experimental results to compare with and validate the numerical peridynamic simulation results.

In this example, the material used is the 1CrMoV steel (Neale 1978), and the material properties are given in Table 1. The plane strain condition is considered, and uniform thickness of $B = 1$ mm is used. Damping is not considered in this example, and the energy balance condition is satisfied during the whole work.

The explicit time integration is utilized in this example. The uniform time step of 50 ns (nanosecond) is used, and it is proven to be the stable time step even for the finest grid size considered. The specimen is loaded by the linearly increasing displacement along the load line as shown in Fig. 3, with a constant speed of 20 mm/s. The total loading time is long enough to ensure that the dynamic effect is negligible before crack propagation. Unlike the standard CT specimen in ASTM E399-12 (2013), there is no physical holes simulated at the position of the loading pin on the CT specimen as shown in Fig. 3, and the displacement load is applied on the nodes located within $1 \text{ mm} \times 1 \text{ mm}$ square centered at the position of the loading pin. Moreover, the no-damage zones are set in the loading areas to avoid the undesired damage because of local effect of loading conditions.

First, the fracture prediction of the CT test is performed with the proposed state-based peridynamic model as $a/w = 0.5$ (Fig. 3), followed by the convergence study (Bobaru et al. 2009). Then, the CT specimens with different values of a/w are considered to quantitatively validate the proposed model for predicting crack propagation problems with different pre-crack lengths.

5.1.2 Fracture behaviors of CT test with $a/w = 0.5$

In this section, a typical initial pre-crack length $a_0 = 20$ mm and the specimen width $w = 40$ mm are used as shown in Fig. 3 which leads to $a/w = 0.5$.

For the numerical peridynamic simulation, the system is discretized into a finite number of nodes with uniform grid spacing. The values of $\delta = 1$ mm and $m = 5$ are first considered to quantitatively analyze the fracture behavior of CT specimen.

The contours of y -direction displacement, damage (crack), and released energy density at the typical time of CT simulation are shown in Fig. 4, where the param-

eter of damage is defined as the volume weight of broken bonds in Silling and Askari (2005). As the displacement load increases, the y -direction displacement increases linearly and symmetrically (see Fig. 4a, b), and the crack starts to grow at the location of pre-crack tip around 6.0×10^{-3} s (see Fig. 4c), and it grows along the pre-crack direction (see Fig. 4d) because of the symmetry of the geometry and loading condition. Meanwhile, the released energy density emerging at the location of crack starts to grow (see Fig. 4e), and it grows synchronously along with the crack path (see Fig. 4f). As shown in Fig. 4, the distribution of released energy density completely overlaps with the new damage map around both sides of pre-crack, because the released energy density is calculated from all the gathering broken bonds of point in Eq. (24), similar to the definition of damage given in Silling and Askari (2005).

Distributions of elastic strain energy density and released energy density around the crack tip before and after the pre-crack propagation are shown in Fig. 5. As shown in Fig. 5a, the strain energy density is first concentrated at the location of pre-crack tip, and the value of concentrated energy increases with the increasing displacement load before the crack starts to grow (see Fig. 5b, c). As the crack grows, the concentrated location of strain energy density moves with the crack tip, and the values of the concentrated strain energy density are nearly equal (see Fig. 5c, d). Meantime, the released energy density appears before the strain energy density arrives the maximum value (see and compare Fig. 5b, e), and it follows the same concentrated location as that of the strain energy density as the crack grows (see Fig. 5f, g). Comparing Fig. 5d and g, the concentrated location of strain energy density moves its front and overlaps with the head of the released energy density path, and the value and concentrated area size of the released energy density are much larger than those of the strain energy density.

The plots of different energy components changing with the increasing displacement load are shown in Fig. 6. As shown in Fig. 6, the sum of U_e (the strain elastic energy), U_k (the kinetic energy), and W_S (the incremental surface energy) is equal to W_e (the work done by external forces) during the CT simulation. It thus perfectly matches the energy balance condition (Sun and Jin 2013):

$$dW_e = dU_e + dU_k + dW_S \quad (38)$$

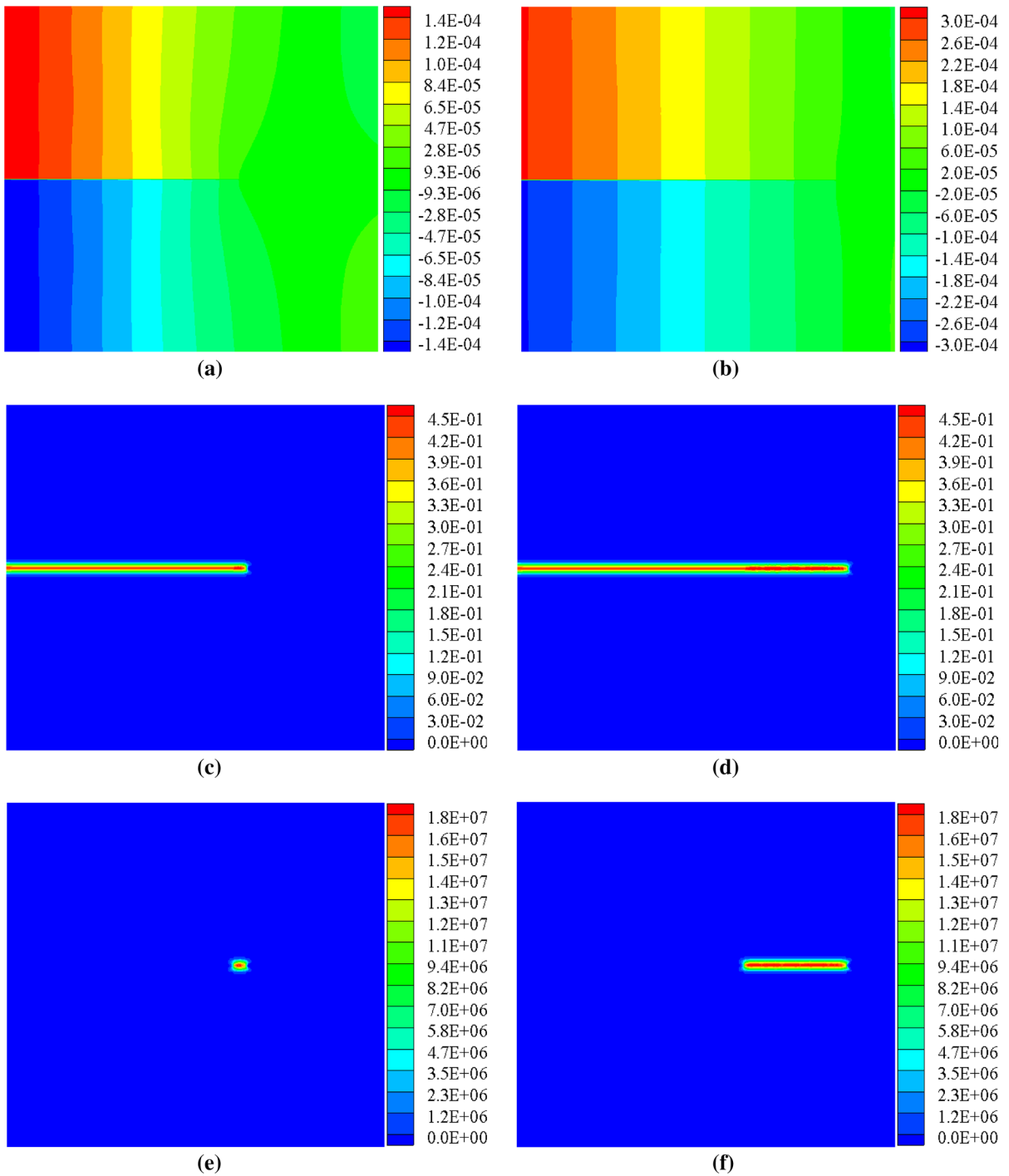


Fig. 4 Contours of y-direction displacement distribution (a and b), damage (c and d), and released energy density (e and f) of CT specimen at crack propagation of 6×10^{-3} s and 12×10^{-3} s,

respectively. **a** At 6×10^{-3} s, **b** At 12×10^{-3} s, **c** At 6×10^{-3} s, **d** At 12×10^{-3} s, **e** At 6×10^{-3} s, **f** At 12×10^{-3} s

Table 1 Material properties for 1CrMoV steel (Reproduced with permission from Neale 1978)

| E (GPa) | ν | ρ (kg/m ³) | K_{Ic} (MPa/m ^{1/2}) |
|-----------|-------|-----------------------------|----------------------------------|
| 214 | 0.27 | 7850 | 64.2 |

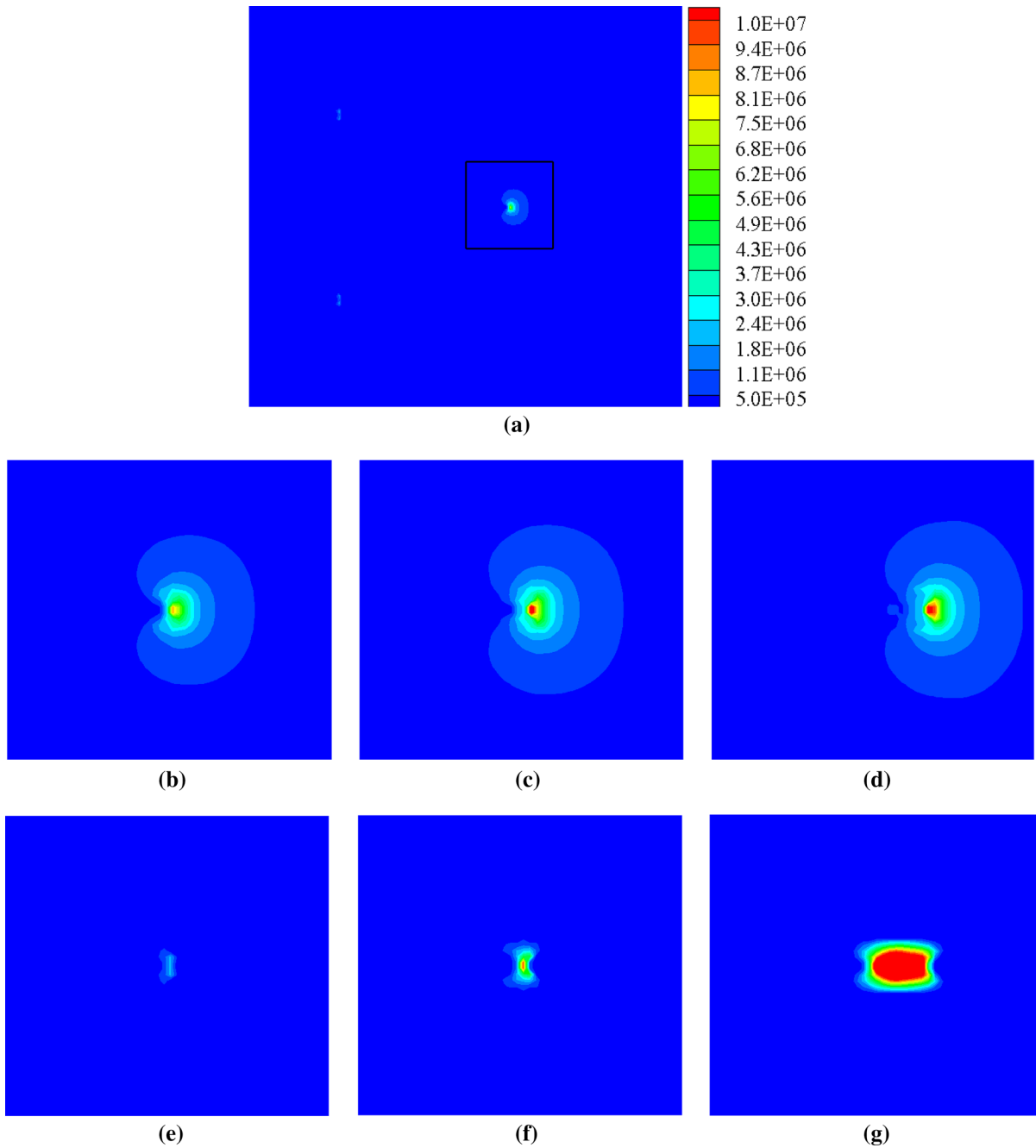


Fig. 5 Distributions of elastic strain energy density (a–d) and released energy density (e–g) around the crack tip area before and after the pre-crack propagates. **a** 4.5×10^{-3} s, **b** 5×10^{-3} s, **c** 5.5×10^{-3} s, **d** 6×10^{-3} s, **e** 5×10^{-3} s, **f** 5.5×10^{-3} s, **g** 6×10^{-3} s

Also as shown in Fig. 6, the kinetic energy of the CT specimen is negligible as compared with the strain elastic energy before the crack starts to grow, which is consistent with the assumption of LEFM considered in the model.

The length of the crack increasing with the displacement load is shown in Fig. 7. As shown in Fig. 7, the velocity of crack propagation (i.e., the slope of the plot) decreases with time. Comparing this curve in Fig. 7 with the plot of incremental surface energy in Fig. 6, two curves have the similar trends. Though the released energy density appears at 4.71×10^{-3} s, the crack does not start to propagate until the total damage energy increases to 3.024×10^{-3} J at the critical time $t_c = 5.26 \times 10^{-3}$ s, which matches the released energy density distribution before the pre-crack starts to propagate (as shown in Fig. 5e). This means that even some bonds of point around the crack tip are broken, the system can still carry the displacement load, which thus confirms the definitions of critical released energy and critical time in Eqs. (30) and (31).

The relationship of Δ_e (the edge opening displacement) and Δ_p (the crack tip opening displacement) during CT simulation are shown in Fig. 8, where Δ_e is equal to V_m in the standard test (ASTM E399-12 2013) and Δ_p is the displacement between two loading tips which is two times of u_y (the displacement load). As shown in Fig. 8, Δ_e increases linearly with the increasing of Δ_p before the crack starts to propagate, and the slope of this region of plot is nearly 0.75. As the crack starts to grow, the slope of the curve decreases with time. The relationship between the edge opening displacement and tip opening displacement before the crack growth matches closely with that given in the experimental CT test (Neale 1978), i.e.,

$$\Delta_e = 0.77\Delta_p \tag{39}$$

The typical load-displacement is given in Fig. 9. As shown in Fig. 9, before crack initiation, the applied load increases linearly with the edge opening displacement, and the value of the reciprocal of slope of this region is 0.214 mm/KN. The value of critical applied load P_c is 1.31 KN, peaked at the critical time t_c . After the critical time, the crack starts to grow and the load drops with the oscillations because of the explicit time integration in transient analysis.

The relationship between the total incremental surface energy W_S and the crack length a as the crack

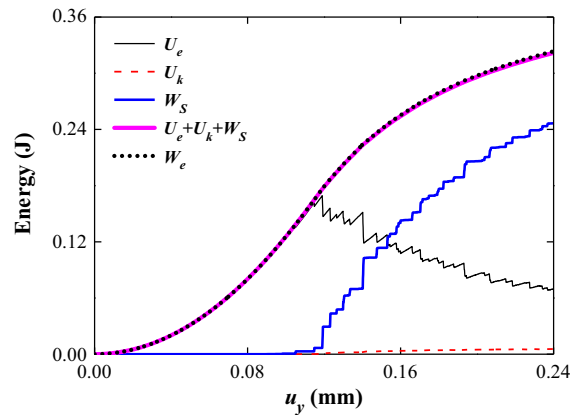


Fig. 6 Different energy components during CT test simulation

grows is shown in Fig. 10, where W_S is equal to the total released energy gathered from the released energy density of system. As a whole, W_S increases linearly with the crack length but in the step-jump form. The value of a step in horizontal axis is the grid size Δx , while the value of a step in vertical axis is nearly equal to the value $GB\Delta x$. To trace the numerical energy release rate as crack propagates, the calculated critical energy release rate G_Q is defined as:

$$G_Q = \frac{\Delta W_S}{B \Delta x} \tag{40}$$

which means that the calculated critical energy release rate G_Q/B is equal to the slope of the plot of W_S vs. a . The value of G_Q in Fig. 10 is 18.50 KJ, as reported in Table 2. Also, at the beginning of the plot, the crack length increases with the incremental surface energy beyond the critical released energy w_s , as defined in Eq. (30).

5.1.3 Convergence study of CT specimen with $a/w = 0.5$

Typical size $a_0 = 20$ mm and $w = 40$ mm are still considered. The convergence study is performed with the horizons of $\delta = 1$ and 2 mm, and $m = 4, 5, 6$, respectively.

First, a fixed horizon size $\delta = 1$ mm and the varying values of $m = 4, 5$ and 6 are used for the m -convergence test. The plots of strain energy density and released energy density around the crack tip area with different values of m are shown in Fig. 11. As shown in Fig. 11, the plots for two different val-

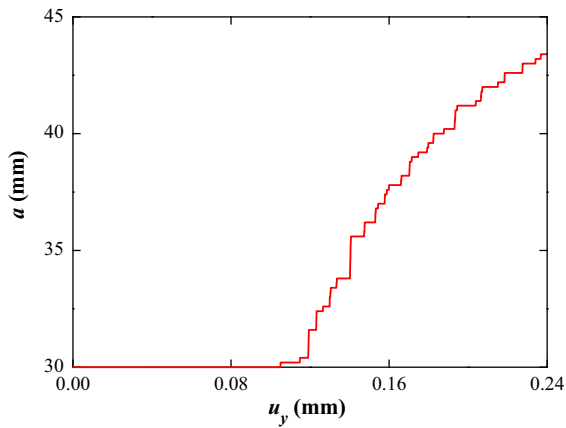


Fig. 7 Crack length versus displacement load during CT test simulation

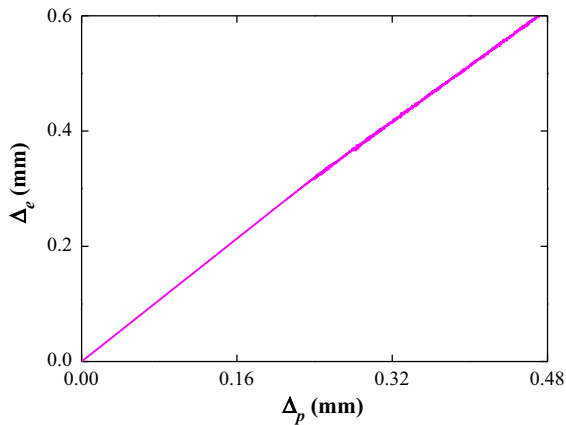


Fig. 8 Edge opening displacement versus tip opening displacement during CT test simulation

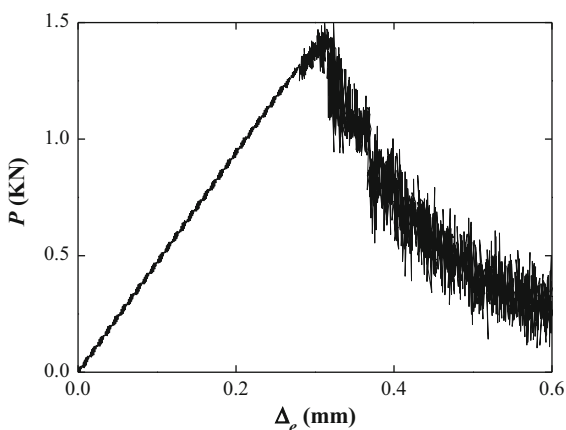


Fig. 9 Applied load versus edge opening displacement during CT test simulation

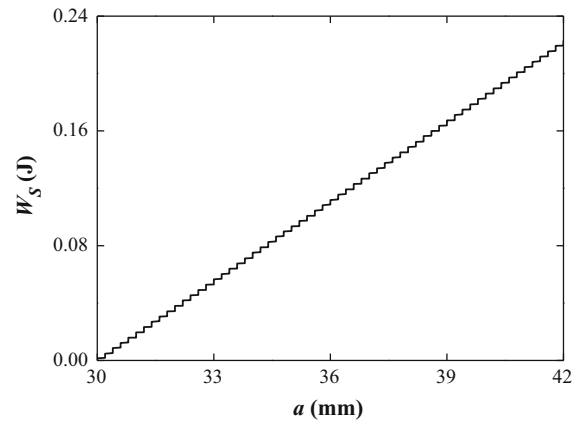


Fig. 10 Incremental surface energy versus crack length as crack propagates

ues of m have the same pattern, and for the larger value of m , the concentrated effect is much obvious. The typical load-displacement plots for different values of m are shown in Fig. 12. As shown in Fig. 12, the plots for different values of m are nearly coincided and have the similar values of slope and critical applied load, which are reported in Table 2. Furthermore, with the increasing value of m , the oscillation effect of curves is weakened when crack propagates.

Then, the fixed value of $m = 5$ is selected to perform the δ -convergence test with the varying values of $\delta = 2$ and 1 mm. The distributions of strain energy density and released energy density around the crack tip area with different values of δ are shown in Fig. 13. As shown in Fig. 13, the damage patterns and strain energy profiles for two different horizons are approximately same. For the smaller value of horizon $\delta = 1$ mm, the concentrated effect of strain energy density and released energy density are more obvious, i.e., the sizes of concentrated area are much smaller and the maximum values are much bigger, which matches the local intensity in fracture mechanics. In addition, the plots of the total incremental surface energy W_S with respect to the crack length a for different values of horizon are shown in Fig. 14. As demonstrated in Fig. 14, two plots with different horizons have the nearly same slope but with different increasing steps. For the smaller value of horizon, the value of a jump

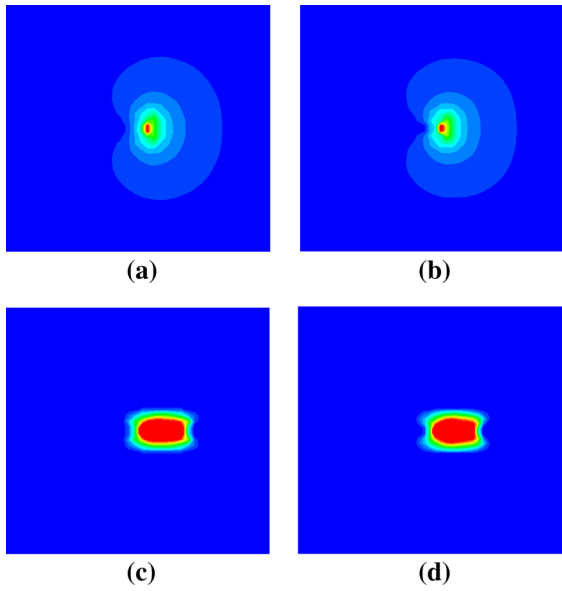


Fig. 11 Strain energy density plots at 5.5×10^{-3} s (**a** and **b**) and released energy density at 6×10^{-3} s (**c** and **d**) around the crack tip area. **a** At 5.5×10^{-3} s ($m = 4$), **b** At 5.5×10^{-3} s ($m = 5$), **c** At 6.0×10^{-3} s ($m = 4$), **d** At 6.0×10^{-3} s ($m = 5$)

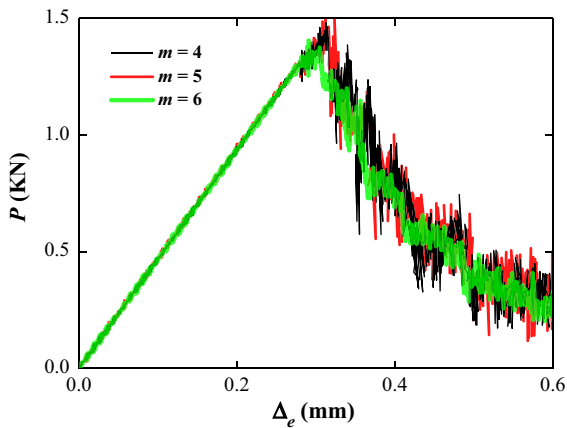


Fig. 12 Applied load versus edge opening displacement for different values of m with $\delta = 1$ mm

step in the plots of Fig. 14 is smaller, and the plot converges to a straight line. The values of slopes are also reported in Table 2.

The simulation results of CT test for different values of δ and m are given in Table 2. As reported in Table 2, the characteristic parameters, i.e., $(\Delta_p)_c$ (the critical load tip opening displacement), $(\Delta_e)_c$ (the critical edge opening displacement), P_c (the critical applied load), Δ_e/P (the crack mouth opening compliance), and G_Q

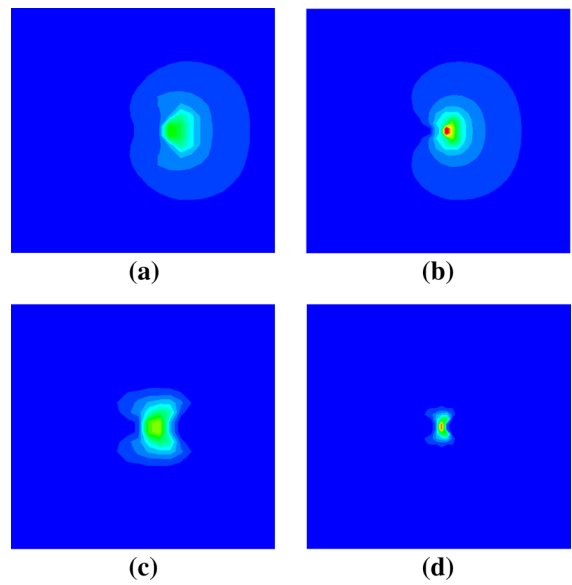


Fig. 13 Strain energy density plots (**a** and **b**) and released energy density (**c** and **d**). **a** $\delta = 2$ mm at 6.0×10^{-3} s, **b** $\delta = 1$ mm at 5.5×10^{-3} s, **c** $\delta = 2$ mm at 6.0×10^{-3} s, **d** $\delta = 1$ mm at 5.5×10^{-3} s

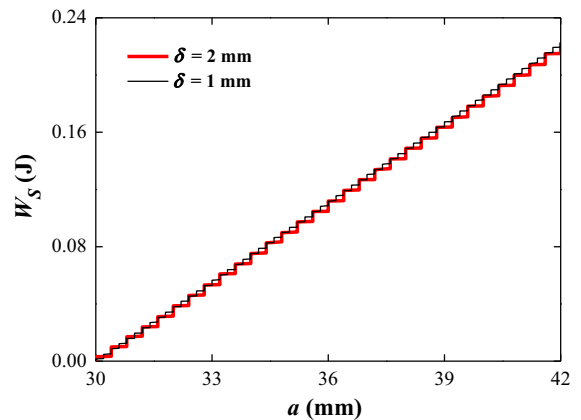


Fig. 14 Incremental surface energy versus crack length for different values of δ with $m = 5$

(the calculated critical energy release rate), are used in this study to quantify the crack initiation and propagation of CT test specimen, and the simulated results are then compared with and verified by those from the standard CT test (ASTM E399-12 2013), as given in Eqs. (33), (35) and (37).

From Table 2, the critical applied load P_c matches closely with the standard values in Eq. (33) with the maximum difference of 3.0%, which means that the peridynamic simulation can successfully predict the critical applied load of CT test. The average value of

compliance is less than that from Eq. (35); however, the maximum difference of crack mouth opening compliance between different values of δ and m is small (less than 4.7%), confirming that the model converges in the elastic region. Since the numerical peridynamic model in Fig. 3 does not exactly emulate the actual standard CT specimen in ASTM E399-12 (2013) which has the loading holes and notch and there is the stiffness enhancement of additional material in the simulation model, the crack mouth opening compliance by the peridynamic model is expectedly less than that of standard experimental model. In addition, the difference of compliance has no effect on the critical applied load which is much important in fracture analysis.

While the critical applied load and crack mouth opening compliance are used to capture the characteristic of CT test before the crack starts to propagate, the calculated critical energy release rate G_Q , as defined in Eq. (40), is employed to validate the effectiveness of the simulation during crack propagation. As shown in Table 2, the maximum difference of G_Q in comparison with the critical energy release rate G_{IC} is less than 3.6%.

5.1.4 Analysis of CT test with different values of a/w

The CT test specimens with different values of a/w are considered to validate the proposed state-based peridynamic (PD) model for predicting the crack initiation and propagation with different pre-crack length.

A fixed specimen width of $w = 40$ mm and different crack length of a_0 increasing from 8 to 32 mm are considered for different values of a/w . According to the convergence study given above, the values of $m = 5$ and $\delta = 2$ mm are used in the following analysis.

The critical applied load and crack mouth compliance for different values of a/w are presented in Figs. 15 and 16, respectively. The critical applied load decreases with the increasing value of a/w , as shown in Fig. 15. Except $a/w = 0.2$, the critical applied loads of peridynamic simulation are close to those from Eq. (33) within a maximum difference of 5.4%, and the difference increases as a/w approaching to 0.2 because of the local effect of the displacement load in the peridynamic model. Meanwhile, the value of crack mouth compliance increases exponentially with a/w , as shown in Fig. 16. The predicted values of crack mouth compliance from the peridynamic model are less than those in Eq. (35); however, the difference decreases as a/w

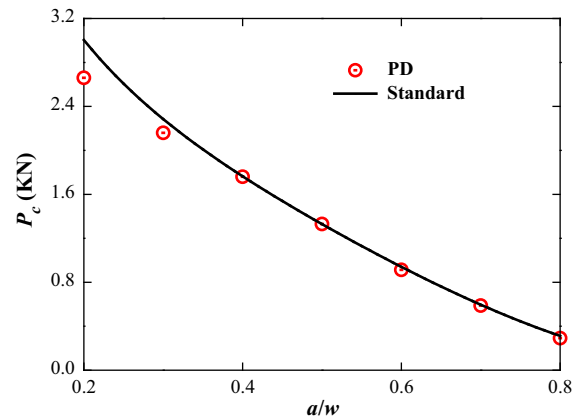


Fig. 15 The critical applied load of CT specimens with different values of a/w

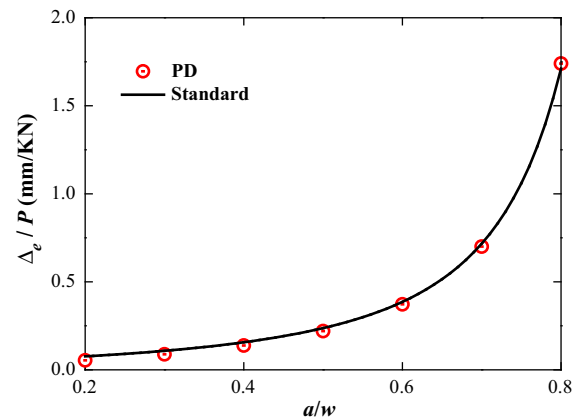


Fig. 16 The crack mouth compliance of CT specimens with different values of a/w

increases, and it is less than 4.0% when a/w increases to 0.6.

As aforementioned, the stiffness in the peridynamic model (see Fig. 3) is higher than that in the experimental CT specimen (ASTM E399-12 2013) which has the loading holes and notch, and it thus leads to larger critical applied load and less crack mouth compliance in the peridynamic simulation. As the value of a/w increases (i.e., the crack length increases), the stiffening effect of material at the location of loading holes and notch on stiffness decreases and the simulation model can thus well capture the critical applied load and crack mouth compliance of CT test specimen.

The quantitative values of simulation characteristic parameters of CT test for different values of a/w are given in Table 3. As shown in Table 3, the val-

Table 2 Peridynamic simulation results for CT test with $a/w = 0.5$

| δ (mm) | 2 | | | 1 | | | ASTM-E-399-12 (2013) |
|----------------------|-------|-------|-------|-------|-------|-------|----------------------|
| | 4 | 5 | 6 | 4 | 5 | 6 | |
| M | | | | | | | |
| $(\Delta_p)_c$ (mm) | 0.224 | 0.242 | 0.222 | 0.210 | 0.210 | 0.215 | |
| $(\Delta_e)_c$ (mm) | 0.292 | 0.292 | 0.289 | 0.280 | 0.280 | 0.286 | |
| P_c (KN) | 1.34 | 1.33 | 1.29 | 1.30 | 1.31 | 1.33 | 1.329 |
| Δ_e/P (mm/KN) | 0.218 | 0.220 | 0.224 | 0.215 | 0.214 | 0.215 | 0.237 |
| G_Q (N/mm) | 17.49 | 18.33 | 18.18 | 17.54 | 18.50 | 18.38 | 17.856 |

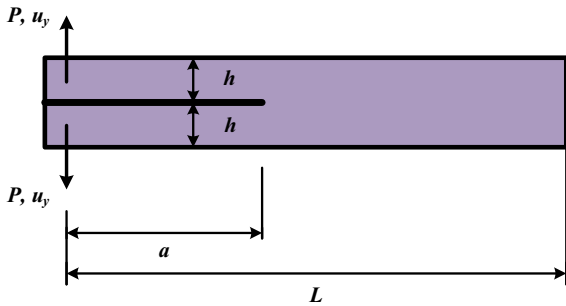


Fig. 17 The DCB specimen

ues of calculated critical energy release rate G_Q for different a/w are close to the input value of G_{IC} ($= 17.856 \text{ N/mm}$), with a maximum difference of 3.1%.

5.2 Double cantilever beam (DCB) test

5.2.1 Problem setup and computational detail for DCB test

Double cantilever beam (DCB) test is a common method to determinate the critical energy release rate of material under mode I fracture loading. As shown in Fig. 17, the special dimensions of DCB specimen are given as: $L = 240 \text{ mm}$, $h = 20 \text{ mm}$, and uniform thickness $B = 10 \text{ mm}$. The properties are chosen to replicate steel (Bidokhti et al. 2017), as reported in Table 4, and the plane stress condition is considered the same as the numerical model based on the finite element method (FEM) in Bidokhti et al. (2017).

The explicit time integration is utilized, and the uniform time step of 200 ns is used. The specimen is loaded with symmetrical and linearly increasing displacement at a constant speed of 20 mm/s, as shown in Fig. 17.

In the DCB specimen simulation, the typical value of initial pre-crack length of $a_0 = 100 \text{ mm}$ is first considered to analyze facture behavior under displacement loading. Then, the critical load analysis of DCB specimens with the different initial pre-crack length a_0 is performed.

5.2.2 Fracture behavior of DCB test with initial pre-crack length $a_0 = 100 \text{ mm}$

The typical initial pre-crack length $a_0 = 100 \text{ mm}$ is first considered. In the peridynamic (PD) model, the system is discretized into uniform grids, and the values of $\delta = 2 \text{ mm}$ and $m = 5$ are considered.

The displacements contours of DCB specimen in deformed shape are presented in Fig. 18. As shown in Fig. 18b, the two sub-beams move symmetrically upward and downward, respectively, with the value of displacement of about 1.2 mm. Meanwhile, the crack starts to grow along the pre-crack direction, and the contours of the crack path, strain energy density, and released energy density around the crack tip area are shown in Fig. 19. As expected, the strain energy density is concentrated at the location of initial pre-crack tip (see Fig. 19b), and the released energy density appears at the crack tip and follows the crack path (see Fig. 19c).

The typical load-displacement plot of DCB test is shown in Fig. 20. As shown in Fig. 20, the peridynamic model successfully captures the load-displacement relationship of DCB test as compared with the FEM results given in Bidokhti et al. (2017). While the curve oscillation appears as the load drops and the crack grows because of the explicit time integration strategy. The values of critical load and displacement are reported in Table 5.

The normalized numerical critical energy release rate of DCB test is also shown in Fig. 21, where G_Q

Fig. 18 Displacements contours of DCB specimen in deformed shape: **a** x component and **b** y component

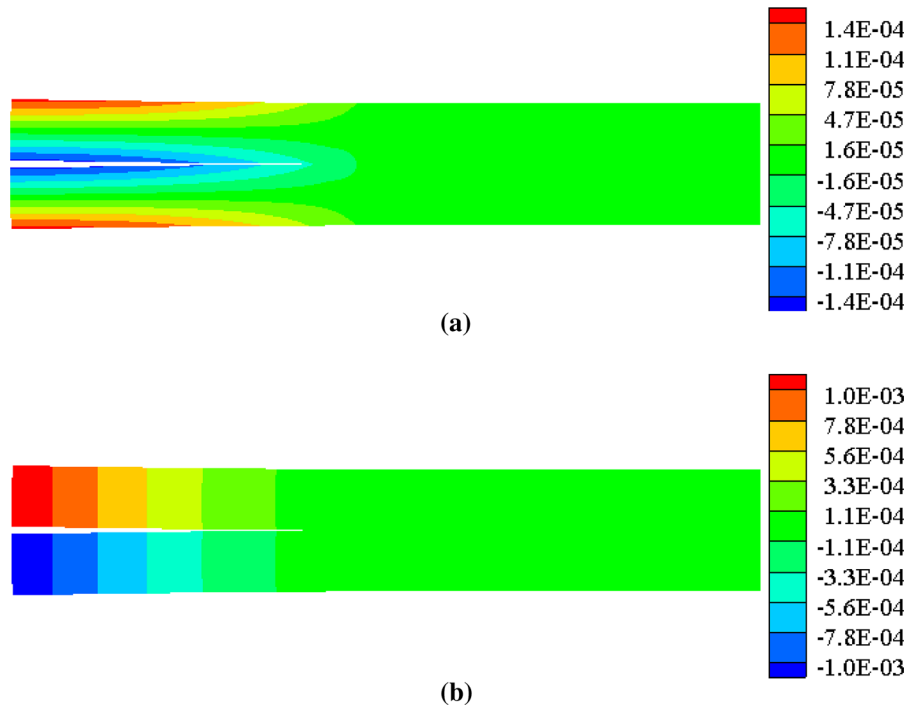


Fig. 19 Simulation of DCB specimen: **a** crack path, **b** strain energy density, and **c** released energy density, around the crack tip at 60×10^{-3} s

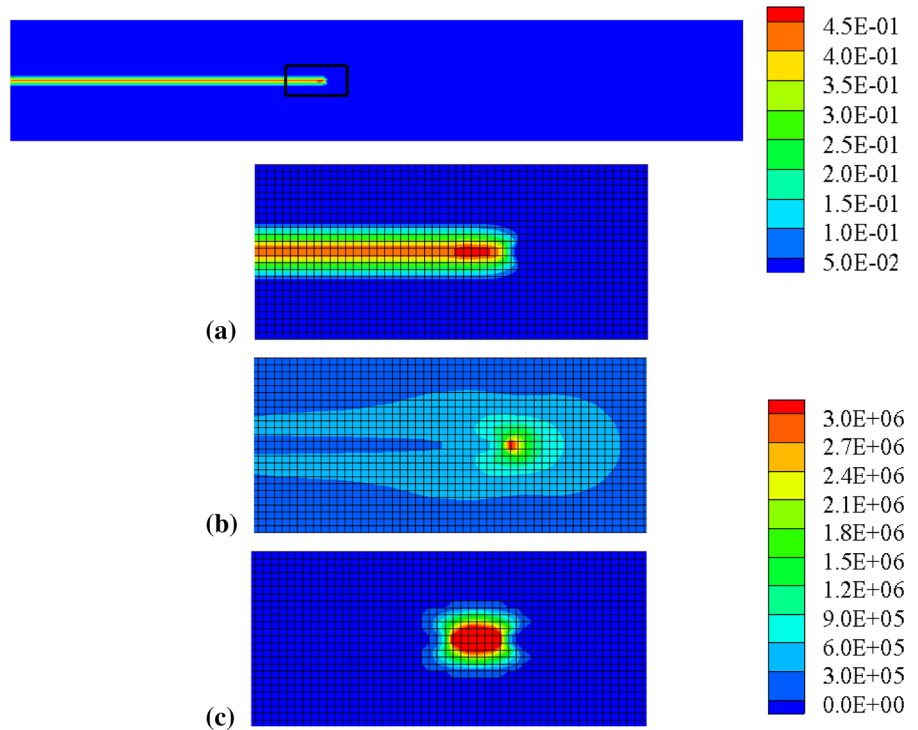


Table 3 Peridynamic simulation results for CT test with different a/w

| a/w | 0.2 | 0.3 | 0.4 | 0.5 | 0.6 | 0.7 | 0.8 |
|----------------------|-------|-------|-------|-------|-------|-------|-------|
| $(\Delta_p)_c$ (mm) | 0.116 | 0.146 | 0.189 | 0.242 | 0.262 | 0.320 | 0.398 |
| $(\Delta_e)_c$ (mm) | 0.142 | 0.187 | 0.243 | 0.292 | 0.340 | 0.412 | 0.508 |
| P_c (KN) | 2.63 | 2.13 | 1.76 | 1.33 | 0.913 | 0.588 | 0.292 |
| Δ_e/P (mm/KN) | 0.054 | 0.088 | 0.138 | 0.220 | 0.372 | 0.70 | 1.74 |
| G_Q (N/mm) | 18.35 | 18.28 | 18.28 | 18.33 | 18.19 | 18.41 | 18.21 |

Table 4 Material properties of steel (Reproduced with permission from Bidokhti et al. 2017)

| E (GPa) | ν | ρ (kg/m ³) | G_{Ic} (N/mm) |
|-----------|-------|-----------------------------|-----------------|
| 200 | 0.3 | 7850 | 9.6278 |

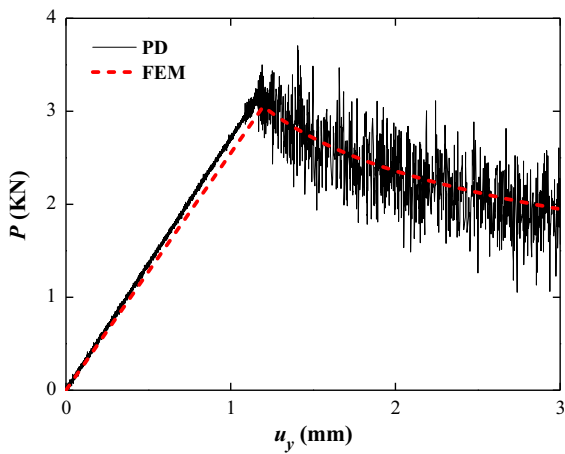


Fig. 20 Applied load versus displacement of DCB specimen with the initial crack $a_0 = 100$ mm

(the calculated critical energy release rate) is calculated using Eq. (40) and normalized by the respective input value (i.e., $G_{Ic} = 9.6278$ N/mm as given in Table 4). As shown in Fig. 21, the calculated critical energy release rate first increases quickly, and then stabilizes with further crack growth, indicating a great match (ASTM D5528-01 2001). The difference between the calculated and input critical energy release rates is less than 1.8% as the crack grows.

5.2.3 DCB test with different values of initial crack length a_0

The different values of initial crack length varying from $a_0 = 100$ to 200 mm are considered. Again, the values

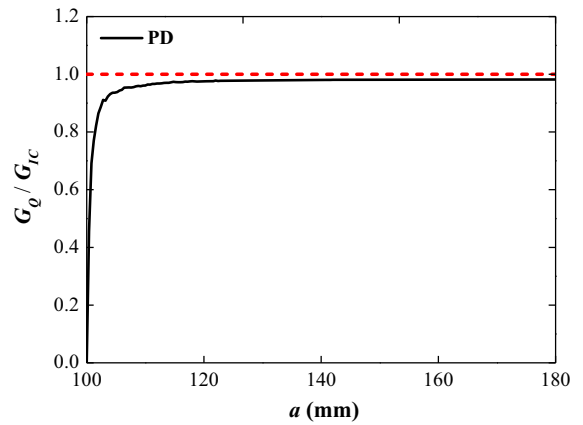


Fig. 21 Numerical critical energy release rate of DCB specimen estimated by the peridynamic model

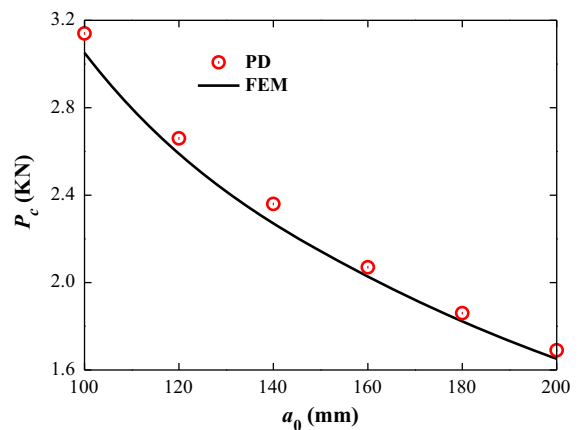


Fig. 22 The critical applied load of DCB specimens with different initial crack length a_0

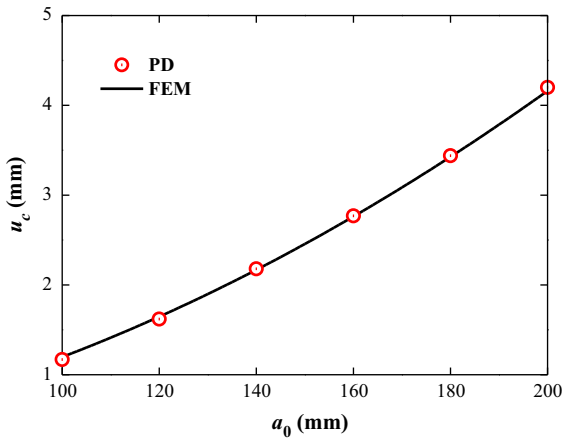


Fig. 23 The critical displacement of DCB specimens with different initial crack length a_0

Table 5 Peridynamic simulation results of DCB test with different initial crack length a_0

| a_0 (mm) | 100 | 120 | 140 | 160 | 180 | 200 |
|----------------|------|------|------|------|------|------|
| $(u_y)_c$ (mm) | 1.17 | 1.62 | 2.18 | 2.77 | 3.44 | 4.20 |
| P_c (KN) | 3.14 | 2.66 | 2.36 | 2.07 | 1.86 | 1.69 |

of $\delta = 4$ mm and $m = 5$ are used in the peridynamic (PD) simulation.

The critical applied load and displacement for different values of initial crack length are presented in Figs. 22 and 23, respectively. As shown in Figs. 22 and 23, with the increasing value of the initial crack length, the critical load decreases and the critical displacement increases. Both the critical load and displacement from the peridynamic model greatly match those from the FEM data within maximum differences of 3.0 and 2.3%, respectively. The values of critical load and displacement of DCB specimens with different initial crack lengths are given in Table 5.

6 Conclusions

In this study, a state-based peridynamic model for fracture analysis is proposed, and the general relationship of the critical stretch and the critical energy release rate is for the first time obtained for the state-based peridynamic model of linear elastic brittle material. This model is utilized to predict the crack initiation and propagation. The commonly used fracture speci-

mens, i.e., compact tension (CT) and double cantilever beam (DCB), are considered, and their fracture tests are investigated. First, the quantitative prediction of crack initiation and propagation and associated convergence study of the CT test are performed with an initial crack length of $a/w = 0.5$, followed by the CT specimen analysis with different values of a/w . Then, fracture behavior of DCB test is analyzed, and the critical load prediction of DCB specimens with different crack length is performed.

In the CT test case, the crack starts to grow at the location of pre-crack tip and grows symmetrically along the pre-crack direction, while the concentrated zones of strain energy moves along with the crack tip. The path of released energy density follows and overlaps the concentrated zones of strain energy. The crack initiation happens at the time of the incremental surface energy ahead of reaching the critical energy release rate, even some bonds around pre-crack tip are already broken. In the convergence study, the denser the grid size, the more obvious the concentrated effects, the smaller the size of concentrated area, the bigger the maximum value of energy density, and the weaker the oscillation of load-displacement curve as crack propagates.

With the increasing value of a/w , the simulated critical applied load decreases and is close to that from the standard equation of Eq. (33) within a maximum difference of 5.4%, except at $a/w = 0.2$, because of the local effect of the displacement load in the peridynamic model. While the simulated crack mouth compliance increases exponentially with the decreasing difference when compared to that from the standard equation of Eq. (35) because of the stiffness enhancement effect of material at the loading holes which is neglected in the peridynamic model. The calculated critical energy release rate also matches closely with the input critical energy release rate value.

In the DCB test case, the two sub-beams deform symmetrically upward and downward, and the crack starts to grow along the pre-crack direction while the strain energy density is concentrated at the location of crack tip. Comparing the simulated load-displacement curve with that from FEM, the peridynamic model successfully captures the load-displacement relationship; while the curve oscillation appears as the load drops and the crack grows because of the explicit time integration strategy. The numerical critical energy release rate of DCB from the peridynamic model also accurately

matches the input critical value. With the increasing length of pre-crack, the critical load of DCB specimen decreases and the critical displacement increases, for which both match closely with FEM.

The proposed state-based peridynamic model for crack quantitatively captures the fracture behavior of the CT and DCB specimen tests. No special fracture criteria are required in the numerical prediction, and the only input parameter for fracture in the proposed state-based peridynamic model is the critical energy release rate of material. The general relationship of the critical stretch and the critical energy release rate Eq. (26) obtained in this study can be used in the framework of state-based peridynamic model to quantitatively analyze fracture behavior of linear elastic brittle materials.

Acknowledgements The authors would like to thank for the partial financial support from the National Natural Science Foundation of China (NSFC Grant Nos.: 51478265 and 51679136) to this study.

References

- ASTM D-5528-01 (2001) Standard test method for mode I interlaminar fracture toughness of unidirectional fiber reinforced polymer matrix composites. Annual book of ASTM standards, vol 15.03. American Society for Testing and Materials, West Conshohocken, PA
- ASTM E-399-12 (2013) Standard test method for linear elastic plane strain fracture toughness K_{IC} of metallic materials. Annual book of ASTM standards, vol 03.01. American Society for Testing and Materials, West Conshohocken, PA
- Baydoun M, Fries TP (2012) Crack propagation criteria in three dimensions using the XFEM and an explicit-implicit crack description. *Int J Fract* 178:51–70
- Belytschko T, Black T (1999) Elastic crack growth in finite elements with minimal remeshing. *Int J Numer Methods Eng* 45:601–620
- Bidokhti AA, Shahani AR, Fasakhodi MRA (2017) Displacement-controlled crack growth in double cantilever beam specimen: a comparative study of different models. *Proc Inst Mech Eng Part C J Mech Eng Sci* 231:2835–2847
- Bobaru F, Yang M, Alves LF, Silling SA, Askari E, Xu J (2009) Convergence, adaptive refinement, and scaling in 1D peridynamics. *Int J Numer Meth Eng* 77(6):852–877
- Foster JT, Silling SA, Chen W (2011) An energy based failure criterion for use with peridynamic states. *Int J Multiscale Comput Eng* 9:675–687
- Gerstle W, Sau N, Silling S (2007) Peridynamic modeling of concrete structures. *Nucl Eng Des* 237:1250–1258
- Ghajari M, Iannucci L, Curtis P (2014) A peridynamic material model for the analysis of dynamic crack propagation in orthotropic media. *Comput Methods Appl Mech Eng* 276:431–452
- Ha YD, Bobaru F (2011) Characteristics of dynamic brittle fracture captured with peridynamics. *Eng Fract Mech* 78:1156–1168
- Hairer E, Lubich C, Wanner G (2003) Geometric numerical integration illustrated by the Störmer-Verlet method. *Acta Numer* 12:399–450
- Hu W, Ha YD, Bobaru F, Silling SA (2012) The formulation and computation of the nonlocal J-integral in bond-based peridynamics. *Int J Fract* 176:195–206
- Hu YL, De Carvalho NV, Madenci E (2015) Peridynamic modeling of delamination growth in composite laminates. *Compos Struct* 132:610–620
- Le QV, Chan WK, Schwartz J (2014) A two-dimensional ordinary, state-based peridynamic model for linearly elastic solids. *Int J Numer Methods Eng* 98:547–561
- Madenci E, Oterkus E (2014) Peridynamic theory and its applications. Springer, New York
- Neale BK (1978) An investigation into the effect of thickness on the fracture behaviour of compact tension specimens. *Int J Fract* 14:203–212
- Silling SA (2010) Linearized theory of peridynamic states. *J Elast* 99:85–111
- Silling SA (2000) Reformulation of elasticity theory for discontinuities and long-range forces. *J Mech Phys Solids* 48:175–209
- Silling SA, Askari E (2005) A meshfree method based on the peridynamic model of solid mechanics. *Comput Struct* 83:1526–1535
- Silling SA, EptonM WO, Xu J, Askari E (2007) Peridynamic states and constitutive modeling. *J Elast* 88:151–184
- Sun CT, Jin Z-H (2013) Fracture mechanics. Academic Press, Waltham
- Xu J, Askari A, Weckner O, Razi H, Silling SA (2007) Damage and failure analysis of composite laminates under biaxial loads. In: 48th AIAA/ASME/ASCE/AHS/ASC structures, structural dynamics, and materials conference, Honolulu, HI, AIAA2007-2315
- Zhang G, Le Q, Loghin A et al (2016) Validation of a peridynamic model for fatigue cracking. *Eng Fract Mech* 162:76–94
- Zhang H, Qiao P (2018) An extended state-based peridynamic model for damage growth prediction of bimaterial structures under thermomechanical loading. *Eng Fract Mech* 189:81–97

Publisher's Note Springer Nature remains neutral with regard to jurisdictional claims in published maps and institutional affiliations.